Understanding Charge Transport in Hybrid Perovskite Thin Films and Devices: Electrical Characterization Methods

Hadi Santoso

Universitas Hasanuddin, Makassar, Indonesia

Dian Permata

Universitas Padjadjaran, Bandung, Indonesia

Agus Wibowo

Universitas Sebelas Maret, Surakarta, Indonesia

Abstract:

The panchromatic light absorption and excellent charge carrier transport properties in organo lead halide perovskites allowed to achieve an unprecedented power conversion efficiency in excess of 25% for thin film photovoltaics fabrication. To understand the underlying phenomena various comprehensive set of optical and electrical techniques have been employed to investigate the charge carrier dynamics in such devices. In this perspective, we aim to summarize the electrical transport properties of perovskite thin films by using (i) impedance spectroscopy (IS), (ii) space charge limited current (SCLC), (iii) field-effect transistors (FETs) and (iv) time-of-flight (TOF) methods. We have deliberated various equivalent circuit used to model the perovskite solar cells by means of IS. The SCLC technique provide vital electrical parameters such as mobility, activation energy, traps density and distribution, carrier concentration, density of states, etc. The TOF technique measures mobility as a primary parameter while the FETs configuration provide a valuable insight into the in-plane charge transport in perovskites thin films. We believe that these notable understanding will provide insights into charge carrier dynamics in perovskite materials and devices.

Keywords: Organo-lead perovskites • charge transport • charge carrier mobility • impedance spectroscopy

1. Introduction

Over the past few years, hybrid organolead halide perovskites has gained momentous attention as a solution processable semiconducting materials to fabricate next generation opto-electrical devices. Owing to excellent opto-electrical properties, organo halide perovskites are found to be superior in some cases to a wide range of established or emerging semiconductors such as: polycrystalline Si, CdTe/CdS, CIGS thin films, organic semiconductors [1-6] and gave properties on par to crystalline silicon (c-Si) and gallium arsenide (GaAs) [7,8]. The attractive features in organolead halide perovskites are: high absorption coefficient ~ 10^5 cm^{-1} [9], excellent charge carrier mobility up to 100 $cm^2V^{-1}s^{-1}$ [10, 11], ambipolar transport [12], low trap density (< 10^{16} cm^{-3}) [13], long carrier diffusion length [14-16] and low exciton binding energy. Altogether these properties have paved the way for thin-film solution processed next-generation opto-electrical devices including, photodetector [12], light emitting diode [17-19], photovoltaics [20-29] field effect transistors (FETs) [30-33]. The unparalled success has been achieved in the field of solar cells and solar-to-electric conversion efficiencey in execess of 25% has been reported in laboratory and is competetive with the existing technology.

Hybrid organic-inorganic perovskite can be represented by generic form of ABX_3, where A is a monovalent organic cation; B is a divalent Pb^{2+} cation; and X is a halide anion (e.g., Cl^-, Br^-, I^- or their mixtures). Methylammonium (MA) lead trihalide [$CH_3NH_3PbX_3$ or $MAPbX_3$] perovskite is a direct-bandgap semiconductor and has been intensively explored for solar cells fabrication. A foremost constituent of flexibility in hybrid organolead halide perovskite is induced by their optical and electrical properties which can be tuned largely accordance to device requirement. By varying the halide ratio in $CH_3NH_3PbX_nY_{3-n}$, one can easily tune the absorption and emission ranges [34, 35]. Furthermore, by replacing MA cation with other organic cations such as ethylammonium or formamidinium (FA) cation, the opto-electrical properties can be tuned [13,30,31,34,36]. Moreover, by varying the halide composition between iodide and bromide in $MAPbI_3$, the bandgap can be tuned between 1.55 and 2.3 eV [32]. Snaith

et al found that the replacement of MA cation in $MAPbI_3$ perovskite with an FA allows to decrease the bandgap to 1.48 eV.

Despite the excellent performances achieved by hybrid perovskites solar cells (PSCs), the basic understanding of the electrical behavior is still limited and lacks in collective opinion among reported electrical transport characteristics of perovskite materials. The objective of the present personal account is to provide insight in the charge carrier dynamics in perovskites thin films. Charge carrier dynamics in perovskites thin films can be probed, either by the transient spectroscopic techniques which does not require direct contact on perovskite films or techniques where electrodes are required to measure the electrical response through the perovskite. Here, we aim to summarize the charge transport properties in organolead halide perovskite thin films investigated by the techniques which required electrical contact. The main techniques discussed in the present perspective are: Impedance spectroscopy, space charge limited current technique, field-effect transistors technique and time-of-flight method.

2. Experimental methods to probed the charge transport in organolead perovskite

2.1. Impedance spectroscopy

Impedance spectroscopy is a sensitive techniques to investigate the various physical process in PSCs. It can provide complete investigation of devices by a single and simple experimental setup. The interfacial recombination processes at the charge extraction layers [i.e. electron transport layers (ETL) or hole transport layers (HTL)] / perovskite interface in PSCs were investigated by many research group. The electrical response of the PSCs in the frequency domain is generally analyzed by fitting to equivalent circuit and important electrical parameters such as resistance, capacitance, time constant etc. can be extracted. A number of equivalent circuit have been proposed to model impedance spectroscopy in PSCs. Bisquert et al. has investigated PSCs using impedance spectroscopy [33]. An uniform approach to adopt an appropriate equivalent circuit to extract the electrical parameters from impedance spectroscopy was

reported [37]. The authors, have evaluated four kinds of equivalent circuits namely (i) Voight, (ii) matryoshka, (iii) Maxwell and (iv) hybrid Voight-matryoshka. The researchers concluded that all these models are suitable to fit the impedance signal of PSCs and nearly provide similar values of the electrical parameters. Out of these model the most frequently model used to fit the impedance response of PSC is given by two-component Voight circuit or linear RC circuit. The Voight circuit contain a series resistance RSer ascribed to contact resistance and an RC element associated to the ionic diffusion, a recombination resistance R1 and a capacitance C1 related to the perovskite dielectric relaxation capacitance featured at low frequency. Another RC element in EC attributed to the charge transport resistance (R2) of the ETL and HTL as well as their interfaces with the perovskite absorber. The capacitance C2 ascribed to the charge accumulation at the interface of perovskite layer and selective contact [38]. This contribution is responsible for the feature appearing at high frequency in the Nyquist plot [39, 40]. Besides the simple series RC circuit the reports are also available on transmission line and Gerischer (G) model for PSCs. The transmission line pattern is generally observed in devices where the charge transport resistance RCt is very small compare to the recombination resistance R_{rec} while if the recombination resistance is smaller than the transport resistance a Gerischer (G) pattern is observed [39-42]. Transmission line is the classical feature seen in dye sensitized solar cells, (DSSCs) and mesostructured PSCs, in which transport is coupled with recombination [41]. Transmission line model was used [33] to analyze the impedance spectroscopy of $MAPbI_3$ based solar cells with two different ETL either nanostructured TiO_2 or ZrO_2. Transmission line feature was noted for electrodes thicker than 2–3 μm while for very thin electrodes transmission line feature was absent. The use of transmission line model (Figure 1a) similar to as in DSSCs (Figure 1b) to investigate the mesoporous TiO_2/$MAPbI_3$/Spiro-OMeTAD based solar cells reported [40]. In this model they introduced additional RC element describing the c-TiO_2 in contact with the perovskite layer instead of the transmission line branch for the m-TiO_2. Moreover, an additional RC element (R_{HTM} and C_{HTM})

was also implemented instead of the Warburg impedance to represents the charge transport inside the HTM to compensate the low hole mobility (Figure 1c).

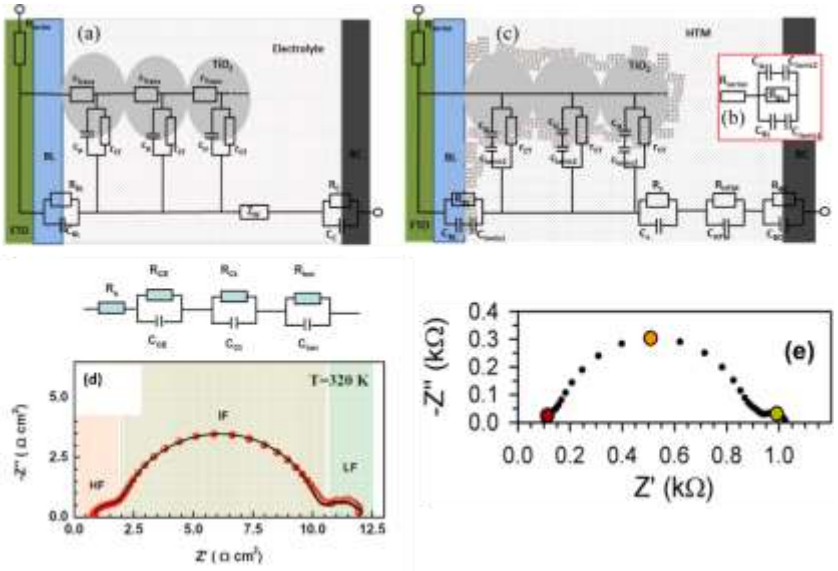

Figure 1. (a) Equivalent circuit of a DSSC (b, c) Full model of a solid-state device with perovskite. Adapted with permission from ref 40. Copyright (2014) American Chemical Society. (d) Top: equivalent circuit for fitting of electronic IS and bottom: IS of c-TiO_2/$MAPbI_3$/Spiro-OMeTAD PSC at 320 K. Adapted with permission from ref 52. Copyright (2015) Royal Society of Chemistry. (e) IS of perovskite solar cell based on $MAPbI_{3-x}Cl_x$ under dark conditions at 0.9 V applied DC bias. Adapted with permission from ref 46. Copyright (2014) American Chemical Society.

A simplified transmission line model [43] was reported to investigate the ambipolar carrier transport and dielectric polarization in perovskite layer. In modified transmission line model, they observed three arcs: at low frequency, intermediate frequency and high frequency which are associated with the dielectric relaxation process, drift-diffusion/recombination, and geometric capacitance in parallel with transport resistances, respectively. The impedance response of planar PSC is much simpler than that of

mesostructured cells. Transmission line behavior was not observed in planar PSCs due to faster transport of carriers through the perovskite films and negligible low frequency effect [44]. Recently, transmission line behavior was also reported for FTO/TiO_2/ $MAPbI_3$/Spiro-OMeTAD [45]. However this model was not found to be very useful to interpret the impedance spectroscopy signal of PSCs as of DSSCs.

The Impedance measurements also provide insight on the polarization of the perovskite material. For instance, three distinguished arc appeared in the impedance plot of PSC based on $MAPbI_{3-x}Cl_x$, shown in Figure 1e [46]. The arc at low, intermediate, and high frequencies are associated to the polarization, chemical capacitance and selective contacts, respectively. i-ZnO as ETL was employed [47] and a semicircle at high frequency was observed, which was assigned to the interfacial charge transfer and recombination while the origin of the arc at low frequency was not clear. Later, they ascribed the low frequency feature to the dielectric relaxation and recombination process in perovskite layer using two component series RC circuit [48,49]. Recently, we have investigated the role of 3−dimensional mesoporous and 1−dimensional TiO_2 nanocolumnar structure on the charge transport properties of c-TiO_2/$MAPbI_3$/Spiro-OMeTAD based PSCs [50]. We have employed two component series RC circuit to extract the high frequency recombination resistance. It was found that the different TiO_2 structure leads to different ideality factors that suggests that electrical properties of perovskite layer depends on the structure of the ETL on which it is deposited. The role of different ETL (TiO_2, ZnO and CdS) was investigated [38] in PSC by using impedance spectroscopy. The authors noted that the transport resistance is dominated by HTL instead of ETL and main recombination pathway is interfacial rather than bulk at low applied bias. Moreover, selective contacts are responsible for the (i) transport resistance at the selector layer, (ii) charge transfer rate at the interface and (iii) surface recombination at the selective contact interface. Impedance spectroscopy of solid state DSSC based on nanocrystals $CH_3NH_3PbI_3$ perovskite absorber layer on top of rutile TiO_2 show a low frequency feature in addition to the two arcs which was attributed to slow charge transport which does not have direct relevance to the device physics [51]. In a

report [52] three arc in impedance measurement was observed and henceforth used three component series R_C-circuit (Figure 1d) to fit the measured impedance signal. They describes the high frequency (100 kHz~600 kHz) arc to the charge exchange (RCE & CCE) process at the Spiro-OMeTAD/Au interface, the semicircle in the intermediate frequency region (50 Hz~100 kHz) to interfacial charge carrier recombination (R_{Ct} & C_{Ct}), and the feature at very low frequencies to the ionic migration (R_{ion} & C_{ion}) inside the perovskite. The charge recombination lifetime evaluated from the relation: $\tau = R_{ct}C$ shows that the recombination lifetime decreases with increasing temperature indicating incomplete dissociation of excitons at low temperature. Moreover, the *J-V* hysteresis effect of such devices becomes weaker below 180K, attributed to the ionic migration and phase transition from tetragonal to orthorhombic phase of perovskite.

The linear series RC model explains the dominant physical processes inside the PSC but were unable to explain the hysteresis resulting from trapping behavior which requires nonlinear RC components [53]. Moreover, the simplified RC circuit cannot provide the mixed electronic/ionic nature of these material and unable to separate the ionic and electronic transport features from each other. An equivalent circuit based on mixed conductor systems shown in Figure 2b was reported [54] and in this model, the low frequency component consists of a charge transfer resistance (R_{CT}) is coupled with Warburg element (W_S) in parallel to interfacial double-layer capacitance (C_{dl}). The capacitance C_{dl} provide the information about charge accumulation at the interface and WS is related to the ion diffusion toward the interface. The chemical capacitance ($C\mu$) represents the total charge stored in the perovskite layer while Relectr ascribed to free carrier recombination/transport (electrons and holes both). Recently, Miyano et al. [55] have introduce a similar equivalent circuit to model the ionic migration in $MAPbI_3$ where they merge the two resistance R_{tr} and R_{Ct} and remove the C_{dl}. The temperature dependence electrical properties of $MAPbI_3$ pellets by means of impedance spectroscopy was investigated [56] and found that the $MAPbI_3$ does not

exhibits ferroelectricity whilst clearly reveal the mixed conducting (i.e. ionic as well as electronic) behavior. To explain the mixed conducting behavior and DC polarization in perovskite, they have added ionic resistance R_{ion} in addition to electronic resistance R_e. But they found this model unable to describe the $\sqrt{t}$ law for short time. Radelli et al. [57] also included the effects of ionic migration in their model (Figure 2d) which produces an additional arc at low frequencies (Figure 2c). In their study they concluded that the low frequency feature is purely related to conductance rather than dielectric effects in contrast to earlier report [16,46]. They found non-ferroelectric contribution are dominant and ruled out the ferroelectricity as the primary source of *J-V* hysteresis observed in PSC. The estimated ionic mobility, ionic conductivities and carrier density in $MAPbI_3$ were in the order of 10^{-10} cm^2 V^{-1} s^{-1}, 10^{-7} Ω^{-1} cm^{-1}, and 10^{20} cm^{-3}, respectively.

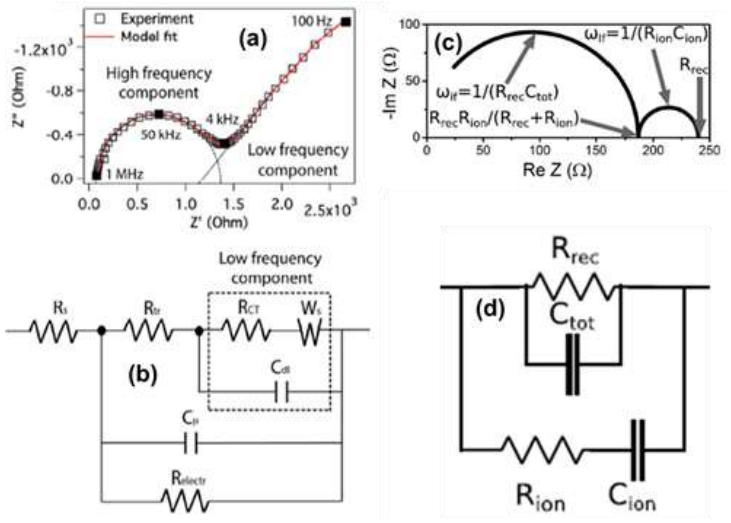

Figure 2 (a) EIS plot of $MAPbI_3$ at 45 °C at 100 $mW.cm^{-2}$ light intensity and 0 V applied bias, (b) equivalent circuit diagram of PSC showing combined charge and ion transport impedance. Adapted with permission from ref 54. Copyright (2015) American Chemical Society. (c) equivalent circuit for our thin films, including the effect of ionic migration and (d) calculated impedance response of the equivalent circuit, using C_{tot} = 14 nF and the experimentally determined parameters R_{rec} = 240Ω; R_{ion} = 840Ω, and C_{ion} = 0:28mF. Adapted with permission from ref 57. Copyright (2015) AIP Publishing.

Fan et al. [58] also found the non-ferroelectric behavior of $MAPbI_3$ in their study by using similar model [56,57] for studying the ionic transport. Temperature dependence impedance spectroscopy experiments shows that the $MAPbI_3$ exhibits different electrical behaviors below 40 °C and above 50 °C, due to the phase transition from tetragonal to cubic structure across this temperature range. The ionic diffusion component also required to fit the impedance spectroscopy of spin coated or sprayed $MAPbI_3$, $FA_{0.85}Cs_{0.15}PbI_3$, and $MAPbBr_3$ films in contact with non-aqueous electrolyte composed of 0.1 M $TBAPF_6$ in CH_2Cl_2 [59].

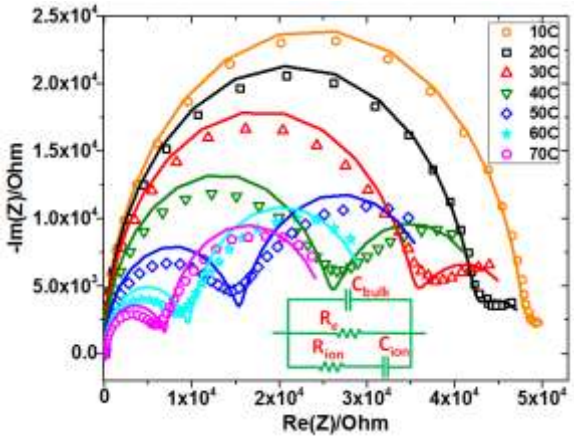

Figure 3. The fittings to the measured IS using the associated model, from which electronic resistance R_e, ionic resistance R_{ion}, geometric and chemical capacitance C_{bulk}, and C_{ion} for contact blocking of mobile ions were extracted The inset shows the equivalent circuit to model the impedance spectrum. Adapted with permission from ref 58. Copyright (2016) American Chemical Society

2.2 Space charge limited current (SCLC) method

The SCLC is a steady-state technique to investigate the charge transport properties of a semiconducting material. In SCLC method, dark current as a function of bias voltage is recorded for a given semiconductor, sandwiched between two metal electrodes. By using SCLC technique, one can easily measure the electron

and hole mobility individually from the quadratic part of the current-voltage (*J-V*) characteristics as shown in Figure 4 through the Mott-Gurney relation [60,61]:

$$J = \frac{9}{8}\varepsilon\mu\frac{V^2}{L^3} \quad (1)$$

where μ, ε and L are the charge carrier mobility, permittivity, and thickness of the perovskite layer, respectively. The technique also provide the information about density of traps and distribution of trap states within the bandgap of semiconductor. The density of deep trap states can be estimated according to the formula [62]:

$$n_{trap} = \frac{2\varepsilon V_{TFL}}{eL^2} \quad (2)$$

where e is the electronic charge and VTFL is the transition voltage from ohmic to trap filling region as shown in Figure 4. In addition, free carrier concentration can be calculated using the relation:

$$n_C = \frac{\sigma}{e\mu} \quad (3)$$

where σ is the conductivity extracted from the ohmic region of *J-V* curve. The measured SCLC carrier mobility and conductivity of $MAPbI_3$ single crystal grown via anti-solvent vapor assisted crystallization (AVC) method was found to be $\mu = 2.5\ cm^2V^{-1}s^{-1}$ and $\sigma = 1\times10^{-8}\ (\Omega\cdot cm)–1$, respectively [63].

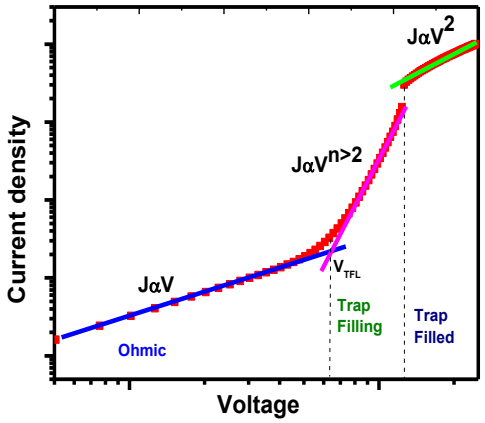

Figure 4. The *J-V* characteristics visualizing different transport regions. A linear ohmic regime ($J \propto V$, blue line) is followed by the trap-filling regime, marked by a steep increase in current ($J \propto V^{n>2}$, purple line).The *J-V* curve shows a trap-free Child's regime ($J \propto V^2$, green line).

The trap density and carrier concentration calculated from above equations were about $n_{traps} \sim 3.3\times10^{10}$ cm^{-3} and $n_C \approx 2\times10^{10}$ cm^{-3}, respectively. In the same work remarkably, higher mobility of $\mu = 38$ cm^2 $V^{-1}s^{-1}$ and low trap density ntraps = 5.8×10^9 cm^{-3} were estimated for $MAPbBr_3$ as compared to $MAPbI_3$ single crystal [63]. The $MAPbX_3$ single crystal grown via a fast crystallization method known as inverse temperature crystallization (ITC) method shows improved electrical properties for $MAPbI_3$ with $\mu = 67.2$ cm^2 V^{-1} s^{-1} and ntraps = 1.4×10^{10} cm^{-3} while slightly deteriorate electrical properties of $MAPbBr_3$ with $\mu = 24.0$ cm^2 V^{-1} s^{-1} and ntraps = 3.0×10^{10} cm^{-3} as compared to those grown via anti-solvent vapor assisted crystallization method [64]. The carrier diffusion length was calculated from the relation:

$$L_D = \sqrt{\frac{\mu \tau k_B T}{e}} \qquad (4)$$

where k_B is the Boltzmann's constant, T is the absolute temperature and τ is the carrier life time. The longest diffusion length was calculated to be ~ 4.3 μm for $MAPbBr_3$ and ~ 10.0 μm for $MAPbI_3$ [64]. Moreover, the authors [12] have also grown $MAPbBr_3$ single-crystal on a planar substrate termed as

planar-integrated single-crystal perovskites. The mobility (μ = 60 $cm^2V^{-1}s^{-1}$) of $MAPbBr_3$ integrated single-crystal perovskite film exhibit orders-of magnitude improvements as compared with the established polycrystalline perovskite films (μ = 0.26 $cm^2V^{-1}s^{-1}$) and equal to those of the best-performing free-standing single-crystal perovskites (μ = 60 $cm^2V^{-1}s^{-1}$) [12]. The calculated carrier diffusion length for free standing crystal, integrated single-crystal film and polycrystalline films were 7.5 μm, 5 μm and 0.3 μm respectively. Huang et al. [65] calculated the carrier diffusion length >175 μm for MAPbI3 single crystal grown via low-temperature solution approach. The trap density in $MAPbI_3$ single crystal (~3.6×10^{10} cm^{-3}) was smaller than the trap density in $MAPbI_3$ polycrystalline thin films (2.0×10^{15} cm^{-3}). The hole and electron mobility of $MAPbI_3$ single crystal were found to be μh = 164 ± 25 cm^2 V^{-1} s^{-1} and μe = 24.8 ± 4.1 cm^2 V−1 s−1, respectively. The electron trap density ntraps = 4.5×10^{10} cm^{-3} was slightly higher compared to the hole trap density. Yang and coworker have grown single crystal of $FAPbI_3$ using a modified inverse temperature crystallization method [66]. The carrier mobility of $FAPbI_3$ single crystal was estimated to be 4.4 cm^2 V^{-1} s^{-1} from quadratic part of J-V characteristics. The defect density in α-phase of $FAPbI_3$ single crystal was 6.2×10^{11} cm^{-3}, which is an order of magnitude higher than that of $MAPbI_3$ single crystal [63-67].

On the other hand the conductivity of $FAPbI_3$ single crystal ~ 1.1×10^{-7} $(\Omega\ cm)^{-1}$ was an order of magnitude higher than that of $MAPbI_3$ single crystal [63] and the calculated carrier concentration was ~1.5×10^{11} cm^{-3}. While mobilities, conductivities, carrier concentrations, and defect density of δ-phase FAPbI3 single crystal were calculated to be μ = 0.179 cm^2 $V^{-1}s^{-1}$, $\sigma = 8.9 \times 10^{-9}$ $(\Omega\ cm)^{-1}$, n = 3.1×10^{11} cm^{-3} , and ntrap = 2.6×10^{12} cm^{-3} , respectively. Both conductivity and mobility of δ-phase $FAPbI_3$ single crystal are lower than α-phase due to the higher bandgap and high defect density in δ-phase than α-phase.

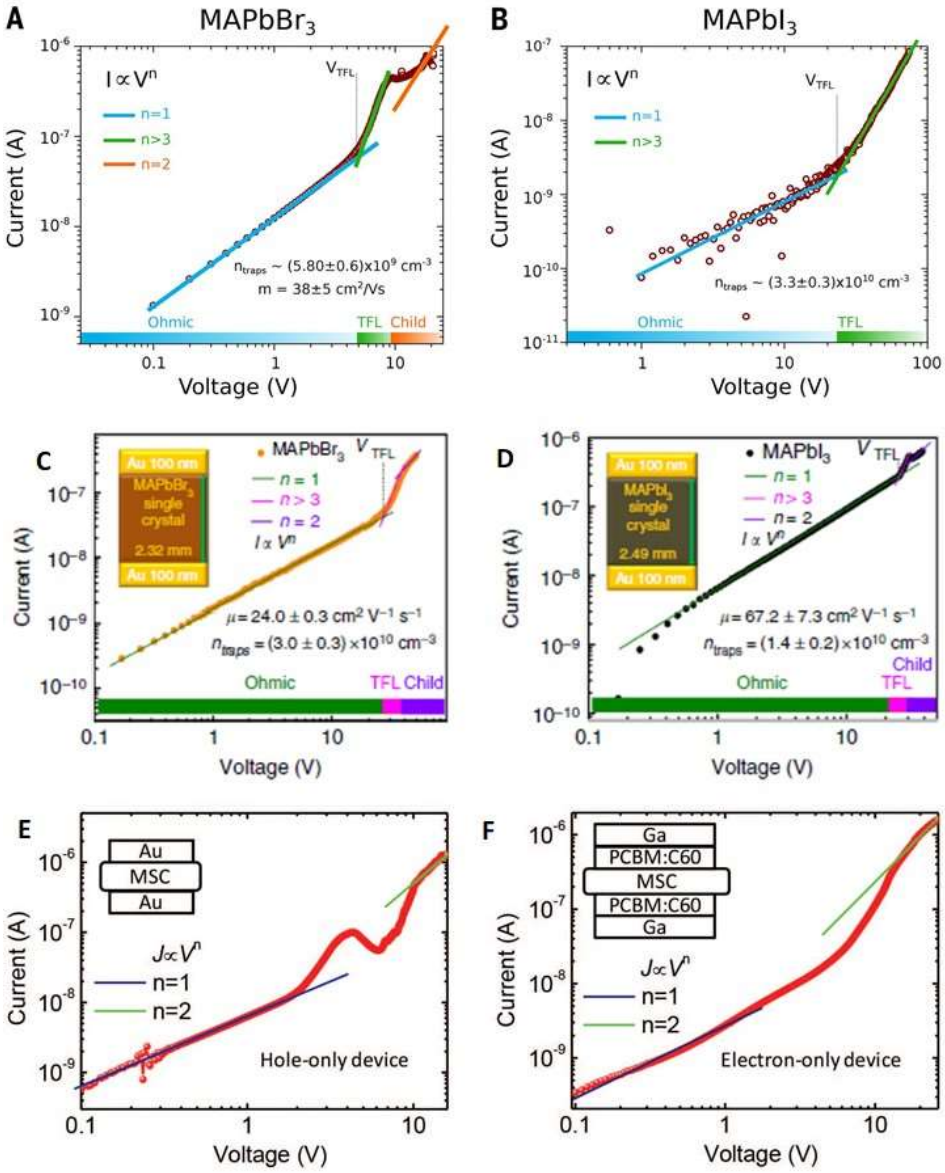

Figure 5. *J-V* characteristic showing three different regimes for (A) $MAPbBr_3$, and (B) $MAPbI_3$ single crystal grown via AVC method. Adapted with permission from ref 63. Copyright (2015) American Association for the Advancement of Science. *J-V* characteristic of (C) $MAPbBr_3$, and (D) $MAPbI_3$ single crystal grown by rapid ITC method Adapted with permission from ref 64. *J-V* curve for (E) a hole-only and (F) an electron-only $MAPbI_3$ single crystal device [65]. Adapted with permission from ref 65. Copyright (2015) American Association for the Advancement of Science.

Adinolfi et al. [68] have used SCLC theory to investigate the electrical properties of $MAPbI_3$ single crystal synthesized by anti-solvent vapor assisted crystallization technique through measuring temperature dependence *I-V* characteristics in both electron- and hole-injecting devices as shown in the inset of Figure 6 a and c, respectively. They have measured a hole mobility of $\mu h \approx 65\ cm^2\ V^{-1}\ s^{-1}$, electron mobility of $\mu e \approx 53\ cm^2\ V^{-1}\ s^{-1}$, free carrier density ~ $4\times10^9\ cm^{-3}$, conductivity ~ $3 \times 10^{-8}\ (\Omega.cm)^{-1}$. The charge carrier diffusion for both electron and hole was found to be same ~ 12 μm. The total traps density at the edge of valence band, was found to be $nt_{VB} \approx 3 \times 10^{10}\ cm^{-3}$ and close to conduction band $nt_{CB} \approx 3 \times 10^{11}\ cm^{-3}$. The density of states (DOS) shows a peak around ≈ 0.2 eV from the conduction band, and at ≈ 0.1 eV from the valence band. Zhumekenov et al. [69] have estimated the electrical parameters for $FAPbX_3$ crystal by using SCLC theory. The measured carrier mobility and conductivity of $FAPbI_3$ crystal were found to be $\mu = 35\ cm^2\ V^{-1}\ s^{-1}$ and $\sigma = 2.2 \times 10^{-8}\ (\Omega\cdot cm)^{-1}$, respectively while the respective parameters for $FAPbBr_3$ crystal were $\mu = 62\ cm^2\ V^{-1}\ s^{-1}$ and $\sigma = 1.5 \times 10^{-8}\ (\Omega\cdot cm)^{-1}$. The trap densities (ntraps) were estimated to 9.6×10^9 and $1.13 \times 10^{10}\ cm^{-3}$ for $FAPbBr_3$ and $FAPbI_3$ crystals, respectively. The free carrier concentration calculated from above equations were about $nC = 1.5 \times 10^9\ cm^{-3}$ and $nC \approx 3.9 \times 10^9\ cm^{-3}$ for $FAPbBr_3$ and $FAPbI_3$ crystals, respectively. The carrier diffusion length was measured to be 19.0 μm for $FAPbBr_3$ and 6.6 μm for $FAPbI_3$ crystal. The electron and hole mobility in metal halide mixed perovskite $MA_{0.60}FA_{0.40}PbI_3$ was estimated to 18.38 $cm^2\ V^{-1}\ s^{-1}$ and 19.96 $cm^2\ V^{-1}\ s^{-1}$, respectively with an diffusion length of 627 ± 9 nm for electron and 504 ± 8 nm for hole [70].

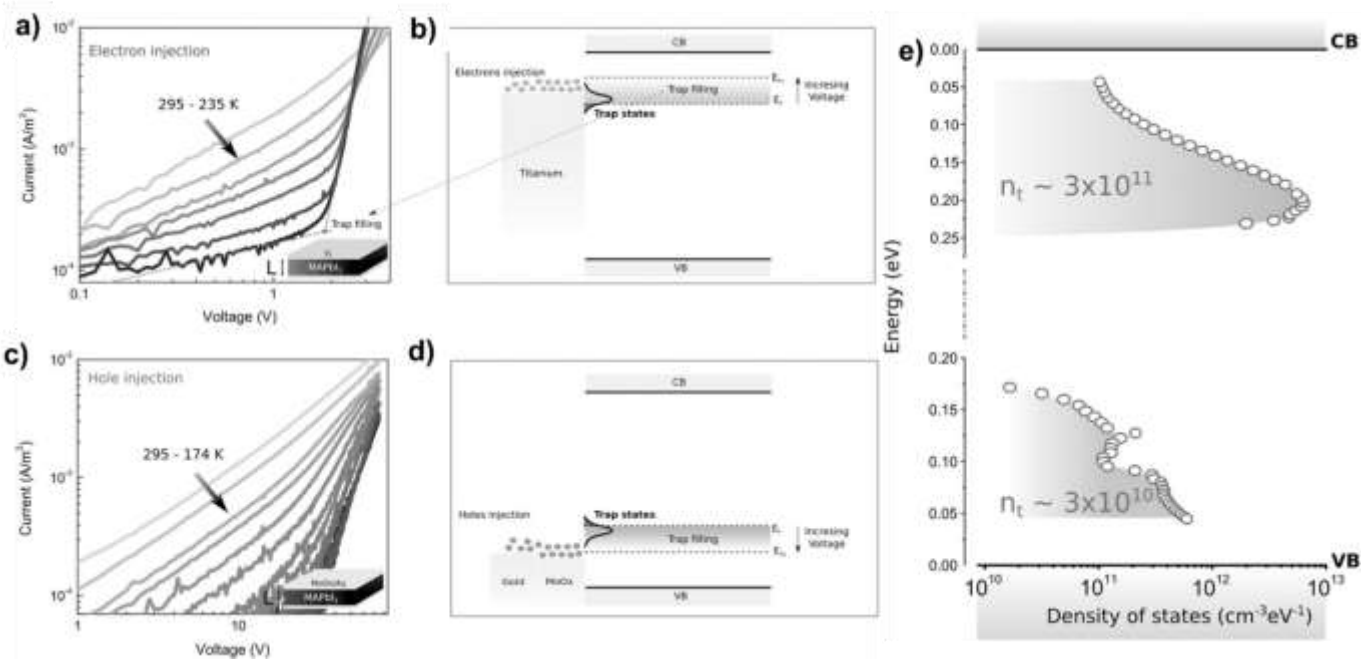

Figure 6. I – V curve as a function of temperature for a MPC in (a) electron and (c) hole injecting devices. Scheme illustrating the principles governing the SCLC method in the case of (b) electrons-injection. (d) hole-injection (e) Density of the trap states within the bandgap of MAPbI3 single crystal. Adapted with permission from ref 68. Copyright (2016) John Wiley and Sons.

The influence of monovalent cation halide addition, including CuI, NaI and AgI on hole mobility of $MAPbI_3$ by using SCLC method [71] was investigated. The electron and hole mobility of pristine perovskite films were estimated to 0.02 $cm^2\ V^{-1}\ s^{-1}$ and 0.008 $cm^2\ V^{-1}\ s^{-1}$, respectively. The NaI-based perovskite thin films exhibits an increase of hole mobility up to an order of magnitude (0.07 $cm^2\ V^{-1}\ s^{-1}$) as compared to the pristine perovskites and electron mobility increases to around 0.04 $cm^2\ V^{-1}\ s^{-1}$, resulting in a balanced charge transport. Correspondingly, the conductivity of NaI-based perovskite was also enhanced to 5×10^{-8} Scm^{-1} compared to 10^{-9} Scm^{-1} for pristine films. The increased SCLC hole mobility in additive-based perovskite films was attributed to a decrease of activation energy for hole transport from 198 to 137 meV and electron transport from 135 to 77 meV. Due to cation doping, the carrier concentration increases which result in filling up of the traps at the transport level and decrease

the barrier for transport which can diminish the activation energy. In another report, authors have introduced the tetracene layer between perovskite and Spiro−OMeTAD in a similar configuration (Fig. 7A) for SCLC measurement [72]. Significant improvement in the current density and decrease in activation energy was noted for tetracene-Spiro devices compared to Spiro-only or tetracene-only devices as shown in Fig. 7C. The variation in the current density and activation energy was attributed to the decreased injection barrier for hole transport due to the graded energy levels of tetracene and Spiro as shown in Figure 7B.

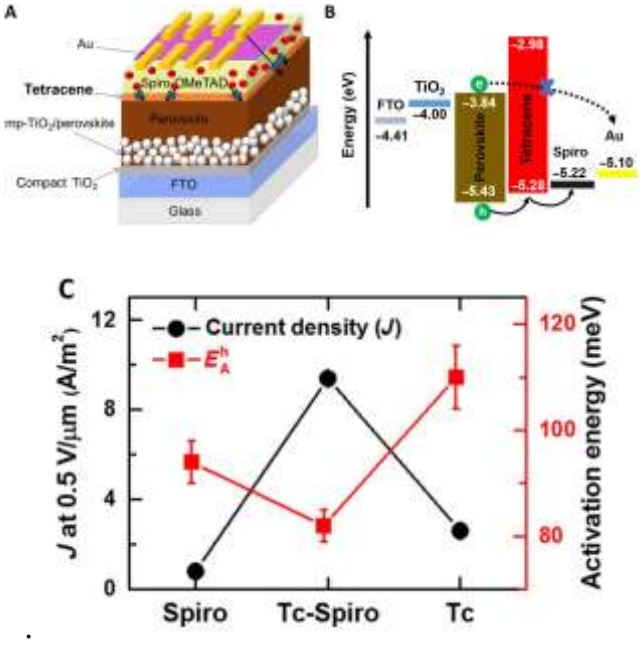

Fig. 7. (A) A device architecture schematic (B) energy-level diagram and (C) trends in current density and activation energy for Spiro-, tetracene-Spiro–,and Tc-based devices. Adapted with permission from ref 72. Reprinted with permission from AAAS.

2.3 Time of flight (TOF) method

In time-of-flight measurement techniques, the perovskite layer is sandwiched between two electrodes. The free charge carriers are generated near to the semitransparent electrode by excitation from a light

pulse. The photogenerated free carriers are then driven under the influence of applied bias (V) giving rise to an instantaneous current. When the carriers reach to the collecting electrode, at time ttr, which is called the transit time, the current decays. The time taken by these carrier to drift through a specified distance d is measured through an oscilloscope as shown in Figure 8. The drift mobility of charge carriers can be calculated from the relation [73]:

$$\mu = \frac{v}{E} = \frac{d^2}{V \times t_{tr}} \quad (5)$$

The TOF technique provide several advantages over other techniques. Here, mobility is measured as a primary parameter rather than deriving from any other parameter. The mobility of electrons or holes can be measured separately in same device by changing the polarity of electrodes. Moreover, the distribution of shallow and deep traps in perovskites can be clearly differentiated by observing different plateaus in TOF, I–t curves. The drift mobility of $MAPbI_3$ thin film in two different device configuration by using a 660 nm diode laser was [74] measured. In device configuration FTO/TiO_2/$MAPbI_3$/poly(3-hexyl)thiophene/Au the hole drift mobility was about 0.18 cm^2/Vs. For device configuration viz. FTO/TiO_2/$MAPbI_3$/Spiro-OMeTAD/Ag the drift mobility was decreased to 0.06 cm^2/Vs. The authors noted that the drift mobilities were dispersive (time-dependent) and the dispersion parameters were in the range of $0.4 - 0.7$, and suggested that terahertz domain mobilities will be much larger than nanosecond domain mobilities.

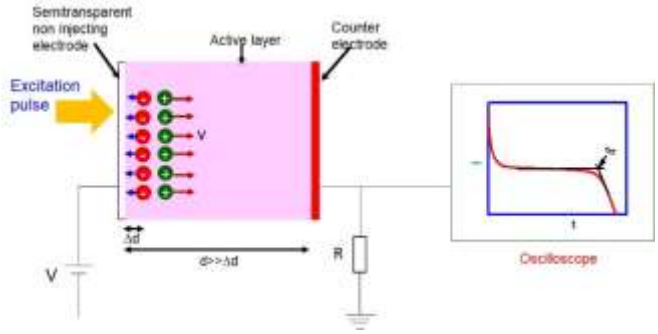

Figure 8. Schematic of the principle of TOF experiment.

Perovskite films was grown [75] via pre-crystallization of an intermediate phase based on a lead-acetate trihydrate precursor mixture in a highly polar solvent. The developed films show charge transport properties similar to those found in perovskite single crystals with electron and hole mobility of 15 cm^2 V^{-1} s^{-1} and 17 cm^2 V^{-1} s^{-1}, respectively as measured through TOF technique. With increase of grain size, the charge carrier mobility values increases, suggesting improved transport properties due to reduction in grain boundaries numbers which represents potential recombination sites. The effect of Cs- and Rb-doping [76] was investigated on the charge transport properties in the mix perovskite $FA_{0.83}MA_{0.17}Pb(I_{0.83}Br_{0.17})_3$ (FAMA) by using TOF technique. The hole and electron mobility in FAMA was estimated to 10 cm^2 V^{-1} s^{-1} which slightly increases for Cs- doped FAMA (μh = 11 cm^2 V^{-1} s^{-1} μe = 12 cm^2 V^{-1} s^{-1}), and Rb- doped FAMA (μ_h = 13 cm^2 V^{-1} s^{-1} μ_e = 14 cm^2 V^{-1} s^{-1}) and a 50% increase was observed for the combination of Rb and Cs (μ_h = 15 cm^2 V^{-1} s^{-1} μ_e = 16 cm^2 V^{-1} s^{-1}). The improve mobility in Cs and Rb-added perovskites attributed to reduced trap density and recombination rate of free carriers. In another report [77] have examined the charge carrier mobilities in $MAPbI_3$ thin films by performing TOF measurements, and noted mobilities values of ~ 6 cm2/Vs for both electrons and holes in MAPI thin films. While in working solar cells the respective mobility values were reduced by three orders of magnitude to 6.2×10^{-3} cm^2 V^{-1} s^{-1}. They concluded that the transport of charge carriers is limited

by thickness of charge extraction layer in particular of HTL Spiro-OMeTAD and less extent to ETL. The influence of chloride on the crystallization of the $MAPbI_3$ and its electrical properties was investigated [78]. The observed that chloride improves the crystal quality and doubles the value of the charge-carrier mobility by extending the evaporation times of the solvent at room temperature. In a similar work [79], authors have investigated effect of the addition of a chloride containing salt to the precursor solution of $MAPbI_3$ films. For chloride-treated perovskite films, they found approximately 34% enhancement in charge carrier mobility of μ=2.16 cm^2 /Vs in comparison to μ=1.62 cm^2 /Vs for untreated $MAPI_3$ films.

2.4 Field-effect transistor (FET) technique

The FET technique allows a precise electrical control over charge density and give a valuable insight into the in-plane charge transport in perovskites. The electrical transport properties of FETs was studied in the device configuration as shown in Figure 9a by recording (i) transfer characteristics I_{DS} vs. V_{GS} and (ii) output characteristics I_{DS} vs. V_{DS}, where V_{DS} is drain voltage, I_{DS} is drain current, and V_{GS} is gate voltage.

The field-effect mobility (μ_{FET}) can be determined from the saturation regime of transfer characteristics from the relationship:

$$I_{DS} = \frac{W}{2L} C_i \mu_{FET} \left[V_{GS} - V_{Th}\right]^2 \quad (6)$$

where, W is channel width, L is channel length, Ci is gate capacitance per unit area. The fabrication of FETs require high

degree of crystallinity to observe the obvious field effect. The ionic migration and ferroelectric polarization in organo-halide perovskite causes electronic screening effect of the applied gate voltage (Figure 9c) [80], yielding a very low room temperature mobility of $\mu_{FET} \sim 10^{-4}$ cm^2 V^{-1} s^{-1} in thin films of $MAPbI_3$ [30]. To eliminate the screening effect, FETs characteristics were recorded at low temperature,

two orders of magnitude increase in both electron (2.1×10^{-2} cm^2 V^{-1} s^{-1}) and hole (7.2×10^{-2} cm^2 V^{-1} s^{-1}) mobilities of $MAPbI_3$ were observed as the temperature reached to 200 K [30]. The mobility in FETs increases with decrease of temperature (Figure 9b) and change in a order of magnitude was recorded around 180 K, which is ascribed to reduced screening effect at low temperature [80]. A significant improvement was noted when methylamine (CH_3NH_2) gas treatment was carried out on $MAPbI_3$ at room temperature [31]. It was found that CH_3NH_2 treatment led to improve the field-effect mobility of $MAPbI_3$ up 22.75 cm^2 V^{-1} s^{-1} due to increase in grain size. The FETs based on $MAPbI_3$ microplate crystals delivered an electron mobility up to 1.0 cm^2 V^{-1} s^{-1} at 77 K, which is higher than those achieved in spin-coated polycrystalline thin films [81-83]. The ambipolar transport in vacuum deposited $MAPbI_3$ FETs was studied [84] and found that the effect of ion migration is not significant in vacuum deposited $MAPbI_3$ films. Additionally, the threshold voltage was found to be far away from zero gate voltage for electron and hole conductions, suggesting that at perovskite/gate dielectric interface, traps are involved in activating ambipolar carrier transport behavior in vacuum-deposited perovskite FETs. Two types of $MAPbI_3$ was fabricated [85], FETs thin films by using (i) PbI_2 and (ii) Pb-acetate precursors. The devices fabricated from the PbI_2 exhibits very poor transistor performance even at low temperature. In contrast, FETs fabricated from the $Pb(Ac)_2$ show an improved transistor performance with an electron mobility of $\mu_{FET} \sim 0.2 \pm 0.08$ cm^2 V^{-1} s^{-1} at 100 K and $\mu_{FET} \sim 0.02 \pm 0.01$ cm^2 V^{-1} s^{-1} at 250 K. In addition, the devices with larger grain size (150 nm) shows field-effect transport even at room temperature and at least one order of higher channel currents than the devices with smaller grain size (38 nm).

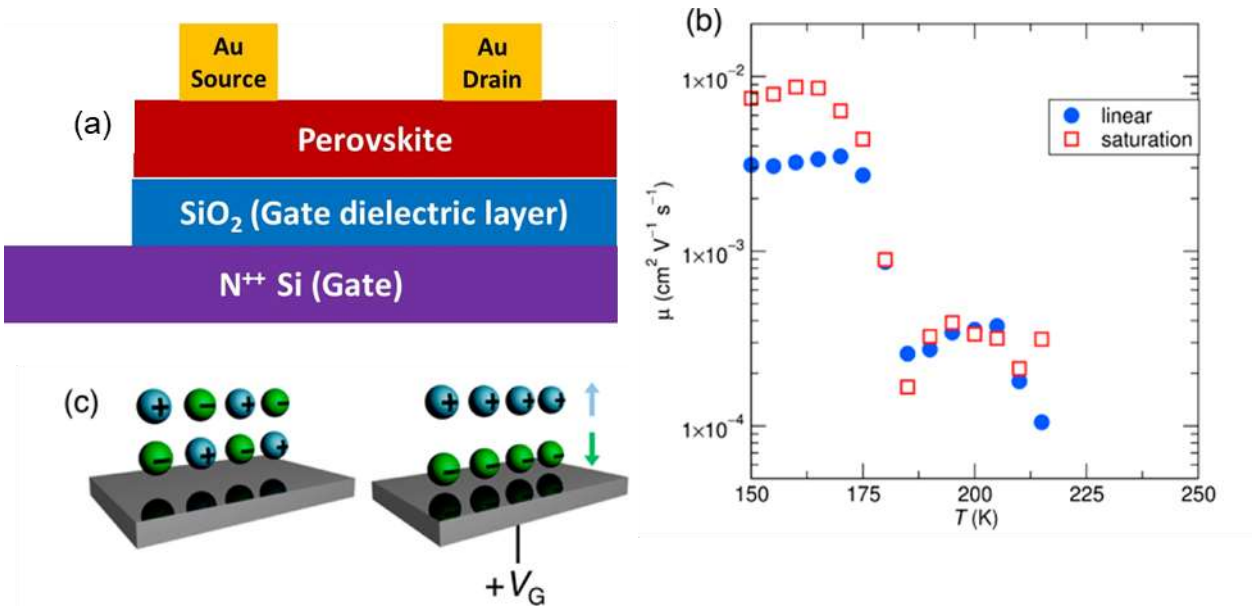

Figure 9 (a) Schematic of bottom-gate, top-contact FETs, (b) field-effect mobility as a function of temperature and (c) schematic representation of screening effect in $MAPbI_3$ perovskite, under the influence of external applied gate field (V_G). Figure b and c are adapted with permission from ref 80. Copyright (2015) American Chemical Society.

Moreover, when an interlayer of pentafluorobenzenethiol (PFBT; ~1 nm thick) or polyethylenimine ethoxylated (PEIE; ~2 nm thick) was introduced between perovskite layer and gold S-D contacts, the μ_{FET} value were enhanced to 2.5 $cm^2\ V^{-1}\ s^{-1}$ at 100K and 0.5 $cm^2\ V^{-1}\ s^{-1}$ at room temperature. Zhang group obtained field-effect mobility as high as of 396.2 $cm^2\ V^{-1}\ s^{-1}$ in $MAPbI_3$ based bottom-gate top-contact, FETs with Ag source and drain (S-D) electrodes [86]. Significantly outperforming room temperature working FETs based on micrometer thin-film $MAPbI_3$ single crystal synthesized via inverse temperature crystallization strategy [87] was fabricated. The authors measured a record value of room-temperature field-effect mobility up to 4.7 and 1.5 $cm^2\ V^{-1}\ s^{-1}$ in p and n channel devices, respectively. Moreover, the field-effect mobility in $MAPbCl_3$ (3.8 $cm^2\ V^{-1}\ s^{-1}$) and $MAPbBr_3$ (3.6 $cm^2\ V^{-1}\ s^{-1}$) based devices were slightly smaller than $MAPbI_3$ (4.7 $cm^2\ V^{-1}\ s^{-1}$) based FET. The transport properties of $MAPbI_3$ in the phototransistor device configuration was [87] studied. The phototransistor exhibit ambipolar carrier transport characteristics with highly balanced photo-induced carrier mobilities of 0.18

$cm^2\ V^{-1}\ s^{-1}$ for holes and 0.17 $cm^2\ V^{-1}\ s^{-1}$ for electrons. When $MAPbI_3$ was doped with Cl-, the hole and electron mobilities in mixed perovskites were improved to 1.24 $cm^2\ V^{-1}\ s^{-1}$ and 1.01 $cm^2\ V^{-1}\ s^{-1}$, respectively, attributed to improvement of surface morphology and decrease in surface roughness of the perovskite films. Jurchescu et al. [89] fabricated mixed halide perovskites ($CH_3NH_3PbI_{3-x}Cl_x$), based bottom-contact, top-gated FETs on Au-patterned S-D electrodes. They noted a balanced charge transport with mobilities of $\mu e \sim 1$ $cm^2\ V^{-1}\ s^{-1}$ and $\mu h \sim 1.3$ $cm^2\ V^{-1}\ s^{-1}$. The device with Cytop dielectric, but without the TTFB contact treatment shows lower mobility of the order of 0.1 $cm^2\ V^{-1}\ s^{-1}$. The authors concluded that the charge carrier transport in FET devices is not only related to the quality of the perovskite layer, but also to the processes that occur at the semiconductor/dielectric interface. Jurchescu et al. [90] have observed that when $MAPbI_{3-x}Cl_x$ films were exposed to the vapors of DMF solvent, the electron and hole average mobilities were improved by over ten times. As-cast films exhibited ambipolar transport, with hole mobility $\mu h = 1.8 \pm 0.3$ $cm^2\ V^{-1}\ s^{-1}$ and electron mobility $\mu e = 0.7 \pm 0.2$ $cm^2\ V^{-1}\ s^{-1}$. A gradual increase in mobility was observed when perovskite films were exposed to DMF solvent vapors, reaching average mobilities of $\mu_h = 10 \pm 2.5$ $cm^2\ V^{-1}\ s^{-1}$ and $\mu_e = 10 \pm 3.4$ $cm^2\ V^{-1}\ s^{-1}$ at 80 min solvent annealing time. Further, solvent annealing up to 100 min or longer yielded a decrease in charge carrier mobility of both holes and electrons, and also led to non-operational devices.

The presence of grain boundaries, interfacial contamination, and other defects introduced during the fabrication of polycrystalline perovskites films obstruct field-effect carrier mobility and FET device operation particularly at room temperature. As discussed in SCLC section that single crystals of hybrid perovskites represents higher carrier mobility, longer carrier diffusion length, and lower trap density compared to polycrystalline films. Amassian and co-worker have synthesizes single crystals of different hybrid perovskites ($MAPbX_3$, X= Cl, Br, and I) using ITC method and fabricated FETs devices [87]. The authors reported record room temperature field-effect hole (electron) mobilities as high as 3.8 (0.32), 3.6 (0.26), and 4.7 (1.51) $cm^2\ V^{-1}\ s^{-1}$ for $MAPbCl_3$, $MAPbBr_3$, and $MAPbI_3$, respectively. High carrier mobility is credited to high quality of semiconductor–dielectric interfaces, free of common morphological defects and chemical impurities often found on the surface of hybrid perovskite polycrystalline films. The

high carrier mobility of perovskites leads to high on/off ratio in the range of 10^3 - 10^5 and low turn-on and threshold voltages. Sirringhaus' group [91] fabricated FETs based on $MAPbBr_3$ perovskites and studied the effect of interface engineering by inserting a buffer layer (either PEDOT:PSS or PFBT) between the perovskite and gold top electrodes. The authors noted insertion of buffer layer alleviate the interfacial electrochemical reactions and thus defects in the perovskites films. Moreover, a significant reduced hysteresis in the current–voltage characteristics was recorded in the PFBT-modified devices. The PFBT modification, also led to improve on/off ratio from $10^2 - 10^6$, when compared to the device with unmodified Au electrodes. The anisotropic charge transport properties of $MAPbI_3$ crystal in top-contact, bottom-gate phototransistor devices [92] was studied. To control the orientation and macroscopic morphology of crystal thermal gradient on the growth-substrate was applied. The resultant structure has two distinct observable growth patterns: one along the thermal gradient (main backbones) and other branches that grow perpendicular to the thermal gradient. The field-effect hole mobility (μ_h) along the direction of main backbone exhibit typical ambipolar behavior, with a value of 2.1 ± 0.3 $cm^2\ V^{-1}\ s^{-1}$ at 78 K and 1.3 ± 0.4 $cm^2\ V^{-1}\ s^{-1}$ at 298 K. While lower hole mobility of the order of 10^{-3} $cm^2\ V^{-1}\ s^{-1}$ was measured along the direction normal to the backbone. At an intermediate angle ~30° tilted with respect to the direction of the backbone, the hole mobility were found to be $3.2 \pm 0.7 \times 10^{-2}$ $cm^2\ V^{-1}\ s^{-1}$ at room temperature and increased to $4.3 \pm 0.5 \times 10^{-2}$ $cm^2\ V^{-1}\ s^{-1}$ at 78 K. The authors attributed the anisotropic charge transport to the structural defect where the side branches join. These grain boundaries hinder charge transport more severely when mobilities of carriers measured in a direction normal to the main backbone.

3. Conclusions

To conclude, systematic introduction of electrical contact based various charge transport characterization techniques including (i) impedance spectroscopy, (ii) space charge limited current, (iii) field-effect transistors, and (iv) time-of-flight have been discussed here. We have put forward the merits and peculiarities of each techniques and what parameters can be derived from such measurements. The use of an ideal equivalent circuit is crucial to extract electrical parameters from impedance spectroscopy. The

impedance spectroscopy also provide information about intrinsic properties of perovskite layer such as ionic and electronic transport, polarization, dielectric relaxation, phase transition. Moreover, impedance spectroscopy give the insight of interfacial phenomenon such as charge accumulation, transfer and recombination at perovskite/hole transport layer or electron transport layer interface. By employing impedance spectroscopic techniques, charge accumulation at hole selective interface was found to be higher as compared to the perovskite/electron interface, while mixed perovskites when equated to pure $MAPbI_3$ gave reduced recombination and high carrier mobility [93]. The electron and hole mobility in perovskite thin films can be unravel by using space charge limited current or time-of-flight techniques. The carrier mobility in perovskite thin films has a bearing not only on the intrinsic property of material, growth conditions (processing parameters), but on its structure as well as measuring technique. In addition to mobility, space charge limited current technique also provide information about electrical conductivity, carrier concentration, diffusion length, trap density and their distribution in the band gap. By employing space charge limited current technique the highest mobility of 164 $cm^2 V^{-1} s^{-1}$ and carrier diffusion length of 175 μm were noted for $MAPbI_3$ single crystal. The highest mobility from time-of-flight measurement was recorded is 17 $cm^2 V^{-1} s^{-1}$. To elucidate in-plane charge transport in perovskite thin films, field-effect transistors is the finest technique, however it requires high degree of crystallinity to observe the required field effect. The mobility in field-effect transistors increases with decrease of temperature due to decrease screening effect at low temperature. Moreover, the field-effect transistors exhibit ambipolar carrier transport behavior unlike bipolar characteristics observed from other techniques. The elucidation of electrical parameters such as equivalent circuit, carrier mobility, traps, carrier concentrations, diffusion length, interfacial and recombination resistance, etc. has a direct bearing on the device performance and provide us a treatment guideline to further push the performance or design of new materials. The knowledge gain by probing such parameters is vital to further optimize the interfaces and understand underlying device kinetics.

Acknowledgements

This work has received funding from the European Union H2020 Programme under European Research council Consolidator grant [MOLEMAT, 726360].

References

[1] J. R. Ayres, J. Appl. Phys. 1993, 74, 1787–1792.

[2] I. Capan, V. Borjanović, B. Pivac, Sol. Energy Mater. Sol. Cells, 2007, 91, 931–937.

[3] A. Balcioglu, R. K. Ahrenkiel, F. Hasoon, J. Appl. Phys. 2000, 88, 7175–7178.

[4] L. L. Kerr, S. S. Li, S. W. Johnston, T. J. Anderson, O. D. Crisalle, W. K. Kim, J. Abushama, R. N. Noufi, Solid-State Electron. 2004, 48, 1579–1586.

[5] C. Goldmann, C. Krellner, K. P. Pernstich, S. Haas, D. J. Gundlach, B. Batlogg, J. Appl. Phys. 2006, 99, 034507.

[6] Y. S. Yang, S. H. Kim, J.-I. Lee, H. Y. Chu, L.-M. Do, H. Lee, J. Oh, T. Zyung, M. K. Ryu, M. S. Jang, Appl. Phys. Lett., 2002, 80, 1595–1597.

[7] J. R. Haynes, J. A. Hornbeck, Phys. Rev. 1955, 100, 606–615.

[8] J. A. Hornbeck, J. R. Haynes, Phys. Rev. 1955, 97, 311–321.

[9] M.-G. Ju, J. Dai, L. Ma, and X. C. Zeng, Adv. Energy Mater. 2017, 7, 1700216.

[10] C. S. Ponseca, T. J. Savenije, M. Abdellah, K. Zheng, A. Yartsev, T. Pascher, T. Harlang, P. Chabera, T. Pullerits, A. Stepanov, J.-P. Wolf, V. Sundström, J. Am. Chem. Soc. 2014, 136, 5189-5192.

[11] E. M. Hutter, G. E. Eperon, S. D. Stranks, T. J. Savenije, J. Phys .Chem. Lett. 2015, 6, 3082-3090.

[12] M. I. Saidaminov, V. Adinolfi, R. Comin, A. L. Abdelhady, W. Peng, I. Dursun, M. Yuan, S. Hoogland, E. H. Sargent, O. M. Bakr, Nat. Commun. 2015, 6, 8724.

[13] J. H. Noh, S. H. Im, J. H. Heo, T. N. Mandal, S. Il Seok, Nano Lett. 2013, 13, 1764–1769.

[14] S. D. Stranks, G. E. Eperon, G. Grancini, C. Menelaou, M. J. P. Alcocer, T. Leijtens, L. M. Herz, A. Petrozza, H. J. Snaith, Science 2013, 342, 341-344.

[15] G. Xing, N. Mathews, S. Sun, S. S. Lim, Y. M. Lam, M. Grätzel, S. Mhaisalkar, T. C. Sum, Science 2013, 342, 344-347.

[16] A. R. Pascoe, N. W. Duffy, A. D. Scully, F. Huang, Y.-B. Cheng, J. Phys. Chem. C 2015, 119, 4444.

[17] B. R. Sutherland, S. Hoogland, M. M. Adachi, C. T. O. Wong, E. H. Sargent, ACS Nano 2014, 8, 10947-10952.

[18] G. Xing, N. Mathews, S. S. Lim, N. Yantara, X. Liu, D. Sabba, M. Grätzel, S. Mhaisalkar and T. C. Sum, Nat. Mater. 2014, 13, 476-480.

[19] H. Zhu, Y. Fu, F. Meng, X. Wu, Z. Gong, Q. Ding, M. V. Gustafsson, M. T. Trinh, S. Jin, X.-Y. Zhu, Nat. Mater. 2015, 14, 636-642.

[20] A. Kojima, K. Teshima, Y. Shirai, T. Miyasaka, J. Am. Chem. Soc. 2009, 131, 6050–6051.

[21] J.-H. Im, C.-R, Lee, J.-W. Lee, S.-W. Park, N.-Gyu Park, Nanoscale 2011, 3, 4088-4093.

[22] M.M. Lee, J. Teuscher, T. Miyasaka, T.N. Murakami, H. J. Snaith, Science 2012, 338, 643–647.

[23] J.T. Wang, J.M. Ball, E.M. Barea A. Abate, J.A. Alexander-Webber, J. Huang, M. Saliba, I. Mora-Sero, J. Bisquert, H. J. Snaith, R. J. Nicholas, Nano Lett. 2014, 14, 724−730.

[24] W.S. Yang, J.H. Noh, N.J. Jeon, Y.C. Kim, S. Ryu, J. Seo, S.II Seok, Science 2015, 348, 1234–1237.

[25] S. S. Shin, E. J. Yeom, W. S. Yang, S. Hur, M. G. Kim, J. Im, J. Seo, J. H. Noh, S. Il Seok, Science 2017, 356, 167-171.

[26] W. S. Yang, B. W. Park, E. H. Jung, N. J. Jeon, Y. C. Kim, D. U. Lee, S. S. Shin, J. Seo, E. K. Kim, J. H. Noh, S. Il Seok, Science 2017, 356, 1376–1379.

[27] J. Cao, B. Wu, R. Chen, Y. Wu, Y. Hui, B. ‐ W. Mao, N. Zheng, Adv. Mater. 2018, 30, 1705596.

[28] D. Yang, R. Yang, K. Wang, C. Wu, X. Zhu, J. Feng, X. Ren, G. Fang, S. Priya, S. (Frank) Li, Nat. Commun. 2018, 9, 3239.

[29] D. Luo, W. Yang, Z. Wang, A. Sadhanala, Q. Hu, R. Su, R. Shivanna, G. F. Trindade, J. F. Watts, Z. Xu, T. Liu, K. Chen, F. Ye, P. Wu, L. Zhao, J. Wu, Y. Tu, Y. Zhang, X. Yang, W. Zhang, R. H. Friend, Q. Gong, H. J. Snaith, R. Zhu, Science 2018, 360, 1442-1446.

[30] G. E. Eperon, S. D. Stranks, C. Menelaou, M. B. Johnston, L. M. Herz, H. J. Snaith, Energy Environ. Sci. 2014, 7 982–988.

[31] S. Pang, H. Hu, J. Zhang, S. Lv, Y. Yu, F. Wei, T. Qin, H. Xu, Z. Liu, G. Cui, Chem. Mater. 2014, 26, 1485–1491.

[32] S. D. Stranks, V. M. Burlakov, T. Leijtens, J. M. Ball, A. Goriely, H. J. Snaith, Phys. Rev. Appl. 2014, 2, 034007.

[33] H.-Seon Kim, I. Mora-Sero, V. Gonzalez-Pedro, F. Fabregat-Santiago, E. J. Juarez-Perez, N.-Gyu Park, J. Bisquert, Nat. Commun. 2013, 4, 2242.

[34] H. Yu, F. Wang, F. Xie, W. Li, J. Chen, N. Zhao, Adv. Funct. Mater. 2014, 24, 7102.

[35] B. R. Sutherland, E. H. Sargent, Nat. Photonics 2016, 10, 295–302.

[36] T. M. Koh, K. Fu, Y. Fang, S. Chen, T. C. Sum, N. Mathews, S. G. Mhaisalkar, P. P. Boix, T. Baikie, J. Phys. Chem. C 2014, 118, 16458-16462.

[37] A. Todinova, L. Contreras-Bernal, M. Salado, S. Ahmad, N. Morillo, J. Idígoras, J. A. Anta, ChemElectroChem 2017, 4, 2891-2901.

[38] E. J. Juarez-Perez, M. Wußler, F. Fabregat-Santiago, K. Lakus-Wollny, E. Mankel, T. Mayer, W. Jaegermann and I. Mora-Sero, J. Phys. Chem. Lett., 2014, 5, 680–685.

[39] V. Gonzalez-Pedro, E. J. Juarez-Perez, W. S. Arsyad, E. M. Barea, F. Fabregat-Santiago, I. Mora-Sero, J. Bisquert, Nano Lett. 2014, 14, 888–893.

[40] A. Dualeh, T. Moehl, N. Tétreault, J. Teuscher, P. Gao, M. K. Nazeeruddin, M. Grätzel, ACS Nano 2014, 8, 362–373.

[41] J. Bisquert, J. Phys. Chem. B 2002, 106, 325−333.

[42] J. Bisquert, I. Mora-Sero, F. Fabregat-Santiago, ChemElectroChem 2013, 1, 289–296.

[43] J. Bisquert, L. Bertoluzzi, I. Mora-Sero, G. Garcia-Belmonte, J. Phys. Chem. C 2014, 118, 18983–18991.

[44] A. Pockett, G. E. Eperon, T. Peltola, H. J. Snaith, A. Walker, L. M. Peter, P. J. Cameron, J. Phys. Chem. C 2015, 119, 3456−3465.

[45] L. Lei, S. Zhang, S. Yang, X. Li, Y. Yu, Q. Wei, Z. Ni, M. Li, Nanotechnology 2018, 29, 255201.

[46] R. S. Sanchez, V. Gonzalez-Pedro, J.-W. Lee, N.-G. Park, Y. S. Kang, I. Mora-Sero, J. Bisquert, J. Phys. Chem. Lett. 2014, 5, 2357.

[47] J. Zhang, P. Barboux, T. Pauporté, Adv. Energy Mater. 2014, 4, 1400932.

[48] J. Zhang, E. José Juárez-Pérez, I. Mora-Seró, B. Viana, T. Pauporté, J. Mater. Chem. A 2015, 3, 4909-4915.

[49] J. Zhang, T. Pauporté, J. Phys .Chem. C 2015, 119, 14919–14928.

[50] M. Salado, L. Calio, L. C.-Bernal, J. Idígoras, J. A. Anta, S. Ahmad, S. Kazim, Materials 2018, 11,1073.

[51] H. -S. Kim, J. -W. Lee, N. Yantara, P. P. Boix, S. A. Kulkarni, S. Mhaisalkar, M. Grätzel, N.-Gyu Park, Nano Lett. 2013, 13, 2412−2417.

[52] H. Zhang, X. Qiao, Y. Shen, T. Moehl, S. M. Zakeeruddin, M. Graetzel, M. Wang, J. Mater. Chem. A 2015, 3, 11762-11767.

[53] D. B. A. Rep, M. W. J. Prins, J. Appl. Phys. 1999, 85, 7923.

[54] M. Bag, L. A. Renna, R. Adhikari, S. Karak, F. L.iu, P. M. Lahti, T. P. Russell, M. T. Tuominen, D. Venkataraman, J. Am. Chem. Soc. 2015, 137, 13130–13137.

[55] X. Chen, Y. Shirai, M. Yanagida, K. Miyano, J. Phys. Chem. C, 2019, 123, 3968–3978.

[56] T. Y. Yang, G. Gregori, N. Pellet, M. Grätzel, J. Maier, Angew. Chem. 2015, 127, 8016−8021.

[57] J. Beilsten-Edmands, G. Eperon, R. Johnson, H. Snaith, P. Radaelli, Appl. Phys. Lett. 2015, 106, 173502.

[58] M. N. F. Hoque, M. Yang, Z. Li, N. Islam, X. Pan, K. Zhu, Z. Fan, ACS Energy Lett. 2016, 1, 142−149.

[59] Z. Li, C. C. Mercado, M. Yang, E. Palay, K. Zhu, Chem. Commun. 2017, 53, 2467-2470.

[60] M. T. Khan, A. Kaur, S. K. Dhawan, S. Chand J. App. Phys. 2011, 109, 114509.

[61] M. T. Khan, V. Agrawal, A. Almohammedi, V. Gupta, Solid-State Electron. 2018, 145, 49-53.

[62] K. C. Kao and W. Hwang, Electrical Transport in Solids, (Pergamon, Oxford) 1981.

[63] D. Shi, V. Adinolfi, R. Comin, M. Yuan, E. Alarousu, A. Buin, Y. Chen, S. Hoogland, A. Rothenberger, K. Katsiev, Y. Losovyj, X. Zhang, P. A. Dowben, O. F. Mohammed, E. H. Sargent, O. M. Bakr, Science 2015, 347, 519 - 522.

[64] M. I. Saidaminov, A. L. Abdelhady, B. Murali, E. Alarousu, V. M. Burlakov, W. Peng, I. Dursun, L. Wang, Y. He, G. Maculan, A. Goriely, T. Wu, O. F. Mohammed, O. M. Bakr, Nat. Comm. 2015, 6, 7586.

[65] Q. Dong, Y. Fang, Y. Shao, P. Mulligan, J. Qiu, L. Cao, J. Huang, Science 2015, 347, 967-970.

[66] Q. Han, S.-Hoon Bae, P. Sun, Y.-Tsung Hsieh, Y. (Michael) Yang, Y. S. Rim, H. Zhao Q. Chen, W. Shi, G. Li, Y. Yang, Adv. Mater. 2016, 28, 2253–2258.

[67] J. R. Ayres, J. Appl. Phys. 1993, 74, 1787–1792.

[68] V. Adinolfi, M. Yuan, R. Comin, E. S. Thibau, D. Shi, M. I. Saidaminov, P. Kanjanaboos, D. Kopilovic, S. Hoogland, Z.-Hong Lu , O.M. Bakr, E. H. Sargent, Adv. Mater. 2016, 28, 3406–3410.

[69] A. A. Zhumekenov, M. I. Saidaminov, M. A. Haque, E. Alarousu, S. P. Sarmah, B. Murali, I. Dursun, X.-H. Miao, A. L. Abdelhady, T. Wu, O. F. Mohammed, O. M. Bakr, ACS Energy Letters, 2016, 1, 32–37.

[70] D. Luo, L. Zhao, J. Wu, Q. Hu, Y. Zhang, Z. Xu, Y. Liu, T. Liu, K. Chen, W. Yang, W. Zhang, R. Zhu, Q. Gong, Adv. Mater. 2017, 29, 1604758.

[71] M. Abdi-Jalebi, M. I. Dar, A. Sadhanala, S. P. Senanayak, M. Franckevicius, N. Arora, Y. Hu, M. K. Nazeeruddin, S. M. Zakeeruddin, M. Grätzel, R. H. Friend, Adv. Energy Mater. 2016, 6, 1502472.

[72] M. Abdi-Jalebi, M. I. Dar, S. P. Senanayak, A. Sadhanala, Z. Andaji-Garmaroudi, L. M. Pazos-Outón, J. M. Richter, A. J. Pearson, H. Sirringhaus, M. Grätzel, R. H. Friend, Sci. Adv. 2019, 5 : eaav2012.

[73] K. S. Haber, A. C. Albrech, J. Phys. Chem. 1984, 88, 6025-6030.

[74] B. Maynard, Q. Long, E. A. Schiff, M. Yang, K. Zhu, R. Kottokkaran, H. Abbas, V. L. Dalal, Appl. Phys. Lett. 2016, 108, 173505.

[75] N. Giesbrecht, J. Schlipf, I. Grill, P. Rieder, V. Dyakonov, T. Bein, A. Hartschuh, P. M.-Buschbaum, P. Docampo, J. Mater. Chem. A, 2018, 6, 4822-4828.

[76] Y. Hu, E. M. Hutter, P. Rieder, I. Grill, J. Hanisch, M. F. Aygüler, A. G. Hufnagel, M. Handloser, T. Bein, A. Hartschuh, K. Tvingstedt, V. Dyakonov, A. Baumann, T. J. Savenije, M. L. Petrus, P. Docampo, Adv. Energy Mater. 2018, 8, 1703057.

[77] I. Grill, M. F. Aygüler, T. Bein, P. Docampo, N. F. Hartmann, M. Handloser, A. Hartschuh, ACS Appl. Mater. Interfaces, 2017, 9, 37655–37661.

[78] A. Binek, I. Grill, N. Huber, K. Peters, A. G. Hufnagel, M. Handloser, P. Docampo, A. Hartschuh, T. Bein, Chem. Asian J. 2016, 11, 1199–1204.

[79] I. Grill, K. Handloser, F. C. Hanusch, N. Giesbrecht, T. Bein, P. Docampo, M. Handloser, A. Hartschuh, Sol. Energ. Mat. Sol. Cells, 2017, 166, 269–275.

[80] J. G. Labram, D. H. Fabini, E. E. Perry, A. J. Lehner, H. Wang, A. M. Glaudell, G. Wu, H. Evans, D. Buck, R. Cotta, L. Echegoyen, F. Wudl, R. Seshadri, M. L. Chabinyc, J. Phys. Chem. Lett. 2015, 6, 3565−3571.

[81] G. Wang, D. Li, H. –C. Cheng, Y. Li, C.-Y. Chen, A. Yin, Z. Zhao, Z. Lin, H. Wu, Q. He, M. Ding, Y. Liu, Yu Huang, X. Duan, Sci. Adv., 2015, 1, e1500613

[82] D. Li, G. Wang, H.-C. Cheng, C.-Y. Chen, H. Wu, Y. Liu, Y. Huang, X. Duan, Nat. Commun. 2016, 7, 11330.

[83] D. Li,H. C. Cheng, Y. Wang, Z. Zhao, G. Wang, H. Wu, Q. He, Y. Huang, X. Duan, Adv. Mater. 2017, 29, 1601959.

[84] Y. Park, B. Park, Results in Physics, 2018, 11, 302-305.

[85] P. Senanayak, B. Yang, T. H. Thomas, N. Giesbrecht, W. Huang, E. Gann, B. Nair, K. Goedel, S. Guha, X. Moya, C. R. McNeill, P. Docampo, A. Sadhanala, R. H. Friend, H. Sirringhaus, Sci. Adv. 2017, 3, e1601935.

[86] Y. Wu, J. Li, J. Xu, Y. Du, L. Huang, J. Ni, H. Caia, J. Zhang, RSC Adv. 2016, 6, 16243-16249.

[87] W. Yu, F. Li, L. Yu, M. R. Niazi, Y. Zou, D. Corzo, A. Basu, C. Ma, S. Dey, M. L. Tietze, U. Buttner, X. Wang, Z. Wang, M. N. Hedhili, C. Guo, T. Wu, A. Amassian, Nat. Commun. 2018, 9, 5354.

[88] F. Li, C. Ma, H. Wang, W. Hu, W. Yu, A. D. Sheikh, T.Wu, Nat. Commun. 2015, 6, 8238.

[89] Y. Mei, C. Zhang, Z.V. Vardeny, O.D. Jurchescu, MRS Commun. 2015, 5, 297–301.

[90] A. M. Zeidell, C. Tyznik, L. Jennings, C. Zhang, H. Lee, M. Guthold, Z. Valy, V. Oana, D. Jurchescu, Adv. Electron. Mater. 2018, 4, 1800316

[91] J. Wang, S. P. Senanayak, J. Liu, Y. Hu, Y. Shi, Z. Li, C. Zhang, B. Yang, L. Jiang, D. Di, A. V. Ievlev, O. S. Ovchinnikova, T. Ding, H. Deng, L. Tang, Y. Guo, J. Wang, K. Xiao, D. Venkateshvaran, L. Jiang, D. Zhu, H. Sirringhaus, Adv. Mater. 2019, 1902618.

[92] N. Cho, F. Li, B. Turedi, L. Sinatra, S. P. Sarmah, M. R. Parida, M. I. Saidaminov, B. Murali, V. M. Burlakov, A. Goriely, O. F. Mohammed, T. Wu, O. M. Bakr, Nat. Commun. 2016, 7, 13407.

[93] M. T. Khan, M. Salado, A. Almohammedi, S. Kazim, S. Ahmad, Adv. Mater. Interfaces 2019, 1901193.